

Article

The Electrical Properties of Tb-Doped CaF₂ Nanoparticles under High Pressure

Tingjing Hu ¹, Xiaoyan Cui ^{1,*}, Jingshu Wang ¹, Xin Zhong ¹, Yinzhu Chen ¹, Junkai Zhang ¹, Xuefei Li ¹, Jinghai Yang ¹ and Chunxiao Gao ²

¹ Key Laboratory of Functional Materials Physics and Chemistry of the Ministry of Education, National Demonstration Center for Experimental Physics Education, Jilin Normal University, Siping 136000, China; tjhumars@126.com (T.H.); jingshuwang126@126.com (J.W.); zhongxin@calypso.cn (X.Z.); yinzhuchen126@126.com (Y.C.); junkaizhang126@126.com (J.Z.); xuefeili163@163.com (X.L.); jhyang1@jlnu.edu.cn (J.Y.)

² State Key Laboratory of Superhard Materials, Jilin University, Changchun 130012, China; chunxiaogao126@126.com

* Correspondence: xycuimail@163.com

Received: 9 January 2018; Accepted: 12 February 2018; Published: 15 February 2018

Abstract: The high-pressure transport behavior of CaF₂ nanoparticles with 3 mol% Tb concentrations was studied by alternate-current impedance measurement. All of the electrical parameters vary abnormally at approximately 10.76 GPa, corresponding to the fluorite-cotunnite structural transition. The substitution of Ca²⁺ by Tb³⁺ leads to deformation in the lattice, and finally lowers the transition pressure. The F[−] ions diffusion, electronic transport, and charge-discharge process become more difficult with the rising pressure. In the electronic transport process, defects at grains play a dominant role. The charge carriers include both F[−] ions and electrons, and electrons are dominant in the transport process. The Tb doping improves the pressure effect on the transport behavior of CaF₂ nanocrystals.

Keywords: high pressure; Tb doping; phase transitions; transport properties

1. Introduction

Recently, rare earth (RE)-doped nanomaterials have attracted much attention [1–5], due to their potential applications such as advanced phosphor [6], display monitors [7], light amplification [8], and biological labeling [9,10], etc. Among these host materials, calcium fluoride (CaF₂) is an attractive host for RE doping because of its high transparency in a wide wavelength region and low phonon energy [11–15].

As an important optical and optoelectronic functional material, a thorough study of the electrical transport properties is essential, and the underlying physical transport behaviors, such as charge carrier type and scattering processes, are worthy of exploration. The impedance spectrum measurement method has long been conventional in studies of electrical charge transportation and related physical properties [16–20]. Specially, using the impedance method, the presence of independent pathways for charge transportation in an inorganic material [21], and the mixed electronic and ionic conduction in various organic and inorganic materials have been satisfactorily addressed [22–26]. We have investigated the electrical properties of CaF₂ nanoparticles with Tb concentrations from 1 mol% to 5 mol% at atmospheric pressure, and it was found that the resistance of the sample with a concentration of 3 mol% Tb is the smallest. Therefore, in this work, the electrical properties of CaF₂ nanoparticles with 3 mol% Tb concentrations under high pressure were investigated by alternate-current (AC) impedance measurement up to 26 GPa. The underlying physical transport behaviors were discussed. Additionally,

the pressure effect on the structural and electrical properties of Tb-doped CaF₂ nanocrystals was compared with that of un-doped nanocrystals.

2. Materials and Methods

A diamond anvil cell (DAC) was used to generate high pressure. The detailed configuration of the electrodes and sample has been illustrated in previous works [27–29]. The final microcircuit and the profile of our designed DAC are shown in Figure 1. Pressure was calibrated by using ruby fluorescence. The ruby measurement scale is 100 GPa [30] and the accuracy of our measurement is 0.1 GPa. To avoid additional error on the electrical transport measurements, no pressure-transmitting medium was used. This will cause non-hydrostatic conditions [31]; however, the effects on the transport measurements can be neglected in our experiment pressure range [32].

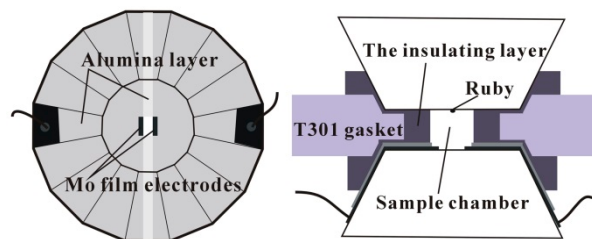


Figure 1. The completed microcircuit (left) on diamond anvil and the profile of our designed diamond anvil cell (DAC) (right).

Impedance spectroscopy was measured by a Solartron 1260 impedance analyzer (Solartron, Hampshire, UK) equipped with a Solartron 1296 dielectric interface. A voltage signal with an amplitude of 1 V was applied to the sample and its frequency ranged from 0.1 to 10^7 Hz.

The sample was prepared by the hydrothermal synthesis method as reported in our previous work [33]. The Tb doping concentrations were 3 mol%. The sample was characterized by transmission electron microscopy (TEM) (JEOL Ltd., Tokyo, Japan) and X-ray diffraction (XRD $\lambda = 1.5406$ Å) (Rigaku, Tokyo, Japan). Figure 2 exhibits the TEM image and the size distribution histogram. It can be seen that the shape of the sample is square with a mean dimension of 8 ± 2 nm.

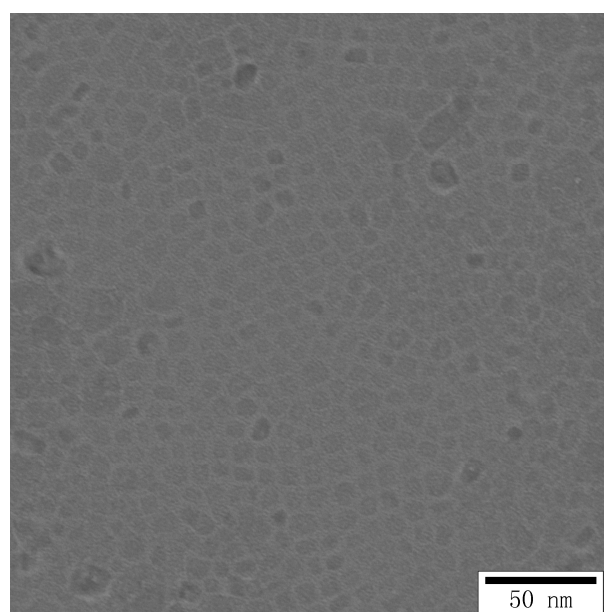


Figure 2. Cont.

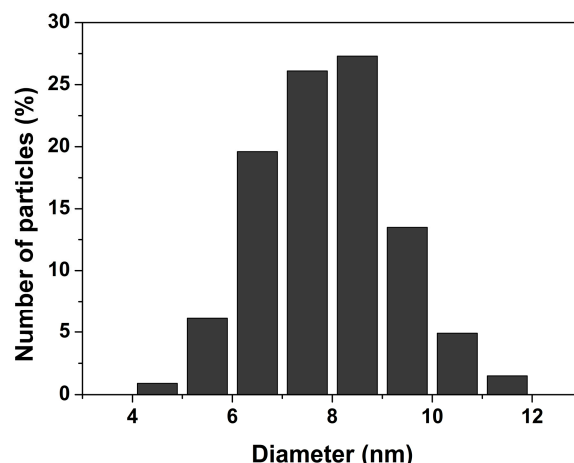


Figure 2. The TEM image and the size distribution histogram of 3 mol% Tb-doped CaF₂ nanoparticles.

3. Results and Discussion

Figure 3 shows the X-ray diffraction pattern of CaF₂ nanoparticles with 3 mol% Tb concentrations. The diffraction peaks of the sample match well with the pure cubic (space group: *Fm3m* (225) $\alpha = \beta = \gamma = 90^\circ$) phase of CaF₂ (Joint Committee on Powder Diffraction Standards JCPDS Card No. 35-0816) and the lattice constant is 5.432 Å, which suggests that the original structure of CaF₂ was retained after doping. No impurity peaks are observed in the pattern, indicating that the Tb³⁺ ions were incorporated into the CaF₂ lattice and substitute Ca²⁺ ions. The average size estimated from the full width at half maximum (FWHM) using the Debye-Scherrer formula is 8.3 nm, which has good agreement with the TEM result.

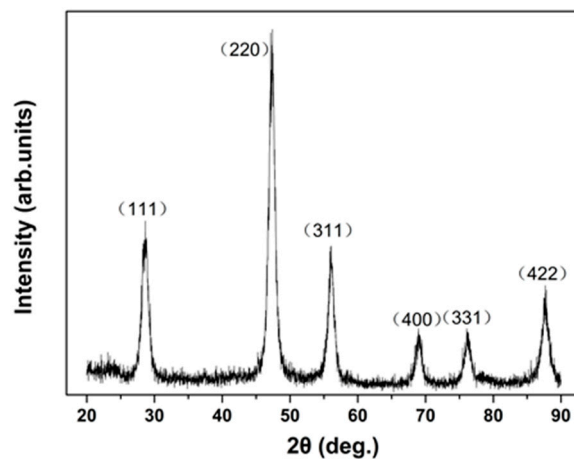


Figure 3. The X-ray diffraction pattern of CaF₂ nanoparticles with 3 mol% Tb concentrations at atmospheric pressure.

The Nyquist impedance spectra of CaF₂ nanoparticles with 3 mol% Tb concentrations under several pressures are presented in Figure 4.

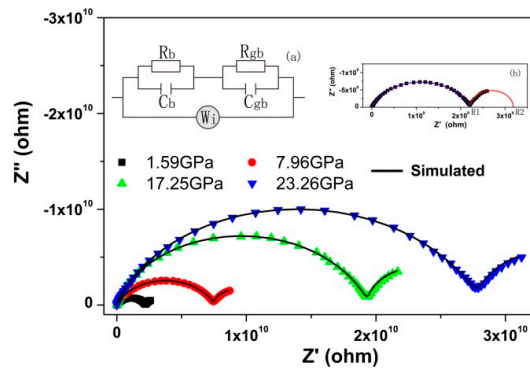


Figure 4. The Nyquist impedance spectra under several pressures. The inset (a) shows the equivalent circuit model, R_b and R_{gb} are grain and grain boundary resistance, C_b and C_{gb} are grain and grain boundary capacitance, and W_i is the Warburg impedance. The inset (b) is the spectroscopy at 1.59 GPa, R_1 and R_2 are two intercepts on the real impedance axis.

To analyze the ionic conduction, the impedance spectra were replotted into $Z' \sim \omega^{-1/2}$ plots, as shown in Figure 5.

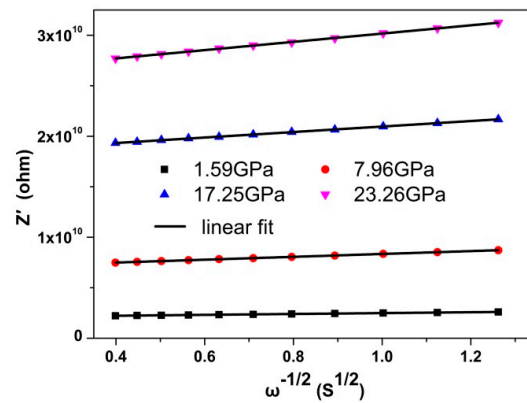


Figure 5. The $Z' \sim \omega^{-1/2}$ curves at low frequencies under several pressures.

In the low frequency region, the Z' can be expressed as:

$$Z' = Z'_0 + \sigma\omega^{-1/2}, \quad (1)$$

where Z'_0 is a parameter independent of frequency, σ is the Warburg coefficient, and ω is the frequency. By linear fitting the $Z' \sim \omega^{-1/2}$ plots, the Warburg coefficient of various pressure was obtained. The diffusion coefficient of the ions (D_i) can be obtained from:

$$D_i = 0.5 \left(\frac{RT}{AF^2\sigma C} \right)^2, \quad (2)$$

where R is the ideal gas constant, T is the temperature, A is the electrode area, F is the Faraday constant, and C is the F^- ions molar concentration. We set the F^- ion diffusion coefficient at 0 GPa as D_0 , and the curve D_i/D_0 under different pressures was obtained and is shown in Figure 6a.

To quantify the pressure effect on the electrical transport properties, the impedance spectra were fitted with the equivalent circuit model (the inset (a) of Figure 4) on the Zview2 impedance analysis software. The obtained bulk and grain boundary resistances (R_b , R_{gb}) are plotted in Figure 6. The relaxation frequency of bulk (f_b) under different pressures was obtained from the $Z'' \sim f$ curve and is presented in Figure 6d.

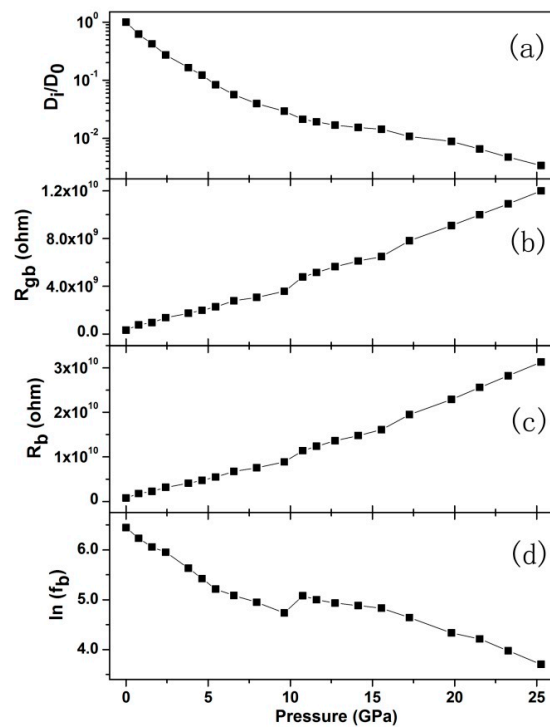


Figure 6. (a) the diffusion coefficient, (b) the bulk resistance, (c) the grain boundary resistance, (d) the bulk relaxation frequency under high pressure. D_0 represents the diffusion coefficient at 0 GPa.

From Figure 6, it can be seen that all of the parameters vary discontinuously at approximately 10.76 GPa, corresponding to the fluorite-cotunnite ($Fm\bar{3}m$ - $Pnma$) structural transition of the sample. According to our previous works [29,33], this phase transition of un-doped CaF_2 nanocrystals occurs at about 14 GPa. The variation in the phase transition pressure with the substitution of Ca^{2+} by Tb^{3+} can be discussed as follows: the ionic radius of Tb^{3+} (0.092 nm) is smaller than that of Ca^{2+} (0.099 nm), and the valence of Tb^{3+} is different with that of Ca^{2+} ; these result in deformation in the lattice and the increasing of the deformation potential, and finally make the transition pressure lower.

In the whole pressure range, the diffusion coefficient decreases with pressure; however, the grain and grain boundary resistance increase, indicating that the F^- ions diffusion and electronic transport become more difficult with the rising pressure. The grain resistance is larger than the grain boundary resistance, which indicates that defects at grains play a dominant role in the electronic transport process.

The pressure dependence of grain activation energy (dH/dP) can be obtained from:

$$d(\ln f_b)/dP = -(1/k_B T)(dH/dP), \quad (3)$$

where k_B is the Boltzmann constant and T is the temperature. By linear fitting to the curve $\ln f_b \sim P$, the dH/dP of the $Fm\bar{3}m$ and $Pnma$ phases were obtained and are listed in Table 1. The dH/dP of un-doped CaF_2 nanocrystals were obtained by the data of Reference [27] and are also shown in Table 1.

Table 1. Pressure dependence of the grain activation energy of Tb-doped and un-doped CaF_2 nanocrystals.

Phase	dH/dp (meV/GPa) (Tb-Doped)	dH/dp (meV/GPa) (Un-Doped)
$Fm\bar{3}m$	4.70	3.12
$Pnma$	2.97	1.44

The positive values of dH/dP in $Fm\bar{3}m$ and $Pnma$ phases indicate that the charge-discharge process becomes more difficult under compression. In the $Fm\bar{3}m$ and $Pnma$ phases, the dH/dP values of the

Tb-doped CaF_2 nanocrystals are larger than those of un-doped CaF_2 nanocrystals. This indicates that pressure has a larger effect on the charge-discharge process of the Tb-doped sample.

To distinguish the contributions of F^- ions and electrons to the transport process, the transference number were calculated by the following equations [34]:

$$t_i = (R_2 - R_1)/R_2, \quad (4)$$

$$t_e = R_1/R_2, \quad (5)$$

where t_i is the transference number of F^- ions, t_e is the transference number of electrons, and R_1 and R_2 are the intercepts on the real impedance axis as shown in the inset (b) of Figure 4. t_i and t_e under various pressures are shown in Figure 7. It can be seen that electrons play a dominant role in the transport process and the electron transference number slightly increases as the pressure rises.

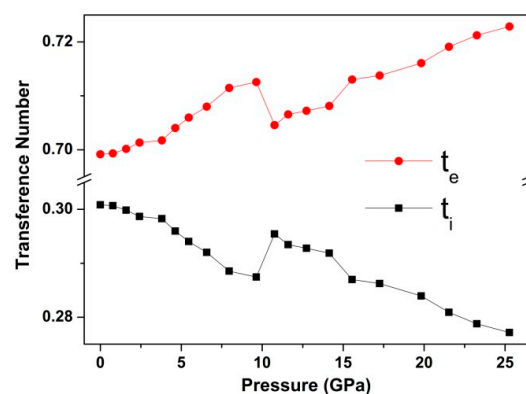


Figure 7. t_i and t_e under various pressures.

To further revealing the effect of Tb doping on the high-pressure transport behavior, the resistance variation of Tb-doped CaF_2 nanocrystals is compared with that of un-doped CaF_2 nanocrystals. The bulk and grain boundary resistances at 0 GPa were set as R_{b0} and R_{gb0} , then the R_b/R_{b0} and R_{gb}/R_{gb0} of Tb-doped and un-doped CaF_2 nanocrystals were obtained and are shown in Figure 8. It can be observed that both in the bulk and grain boundary, the resistance variation of the Tb-doped sample is larger than that of the un-doped sample. This indicates that the Tb doping improves the pressure effect on the transport behavior of CaF_2 nanocrystals.

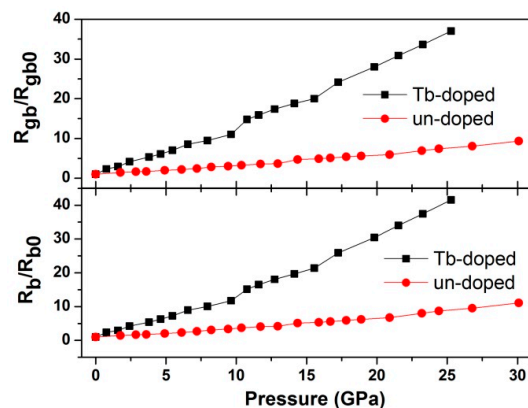


Figure 8. The R_b/R_{b0} and R_{gb}/R_{gb0} of Tb-doped and un-doped CaF_2 nanocrystals. R_{b0} and R_{gb0} represent bulk and grain boundary resistances at 0 GPa.

4. Conclusions

The electrical properties of CaF₂ nanoparticles with 3 mol% Tb concentrations under high pressure were investigated by impedance measurement. All of the electrical parameters vary abnormally at approximately 10.76 GPa, corresponding to the *Fm3m–Pnma* structural transition. The substitution of Ca²⁺ by Tb³⁺ leads to deformation in the lattice, and finally lowers the transition pressure. The F[−] ions diffusion, electronic transport, and charge-discharge process become more difficult with the rising pressure. In the electronic transport process, defects at grains play a dominant role. The charge carriers include both F[−] ions and electrons, and electrons are dominant in the transport process. The Tb doping improves the pressure effect on the transport behavior of CaF₂ nanocrystals. Other lanthanides such as Yb, Er, Ce, etc. would cause similar effects and should be explored in the future.

Acknowledgments: This work was financially supported by the National Natural Science Foundation of China (Grant Nos. 11674404, 11704151 and 11404137), the Twentieth Five-Year Program for Science and Technology of Education Department of Jilin Province, China (Grant No. 20150221), and the Open Project of State Key Laboratory of Superhard Materials (Jilin University) (Grant No. 201710)

Author Contributions: Tingjing Hu conceived and designed the experiments; Jingshu Wang and Yin Zhu Chen fabricated and characterized the sample; Xin Zhong and Junkai Zhang collaborated in XRD, TEM measurements; Xiaoyan Cui, Jinghai Yang and Chunxiao Gao analyzed the data. All authors discussed the experiment results and contributed to writing the paper.

Conflicts of Interest: The authors declare no conflict of interest.

References

1. Bazzi, R.; Flores, M.A.; Louis, C.; Lebbou, K.; Zhang, W.; Dujardin, C.; Roux, S.; Mercier, B.; Ledoux, G.; Bernstein, E.; et al. Synthesis and properties of europium-based phosphors on the nanometer scale: Eu₂O₃, Gd₂O₃: Eu, and Y₂O₃: Eu. *J. Colloid Interface Sci.* **2004**, *273*, 191–197. [[CrossRef](#)] [[PubMed](#)]
2. Nishi, M.; Tanabe, S.; Inoue, M.; Takahashi, M.; Fujita, K.; Hirao, K. Optical-telecommunication-band fluorescence properties of Er³⁺-doped YAG nanocrystals synthesized by glycothermal method. *Opt. Mater.* **2005**, *27*, 655–662. [[CrossRef](#)]
3. Rulison, A.J.; Flagan, R.C. Synthesis of yttria powders by electrospray pyrolysis. *J. Am. Ceram. Soc.* **1994**, *77*, 3244–3250. [[CrossRef](#)]
4. Patra, A.; Friend, C.S.; Kapoor, R.; Prasad, P.N. Fluorescence upconversion properties of Er³⁺-doped TiO₂ and BaTiO₃ nanocrystallites. *Chem. Mater.* **2003**, *15*, 3650–3655. [[CrossRef](#)]
5. Masenelli, B.; Melinon, P.; Nicolas, D.; Bernstein, E.; Prevel, B.; Kapsa, J.; Boisron, O.; Perezl, A.; Ledoux, G.; Mercier, B.; et al. Rare earth based clusters for nanoscale light source. *Eur. Phys. J. D* **2005**, *34*, 139–143. [[CrossRef](#)]
6. Wei, Z.G.; Sun, L.D.; Liao, C.S.; Yan, C.H. Fluorescence intensity and color purity improvement in nanosized YBO₃: Eu. *Appl. Phys. Lett.* **2002**, *80*, 1447–1449. [[CrossRef](#)]
7. Matsuura, D. Red, green, and blue upconversion luminescence of trivalent-rare-earth ion-doped Y₂O₃ nanocrystals. *Appl. Phys. Lett.* **2002**, *81*, 4526–4528. [[CrossRef](#)]
8. Barber, D.B.; Pollock, C.R.; Beecroft, L.L.; Ober, C.K. Amplification by optical composites. *Opt. Lett.* **1997**, *22*, 1247–1249. [[CrossRef](#)] [[PubMed](#)]
9. Yi, G.; Lu, H.; Zhao, S.; Ge, Y.; Yang, W.; Chen, D.; Guo, L. Synthesis, characterization, and biological application of size-controlled nanocrystalline NaYF₄:Yb, Er infrared-to-visible up-conversion phosphors. *Nano Lett.* **2004**, *4*, 2191–2196. [[CrossRef](#)]
10. Chen, Z.; Chen, H.; Hu, H.; Yu, M.; Li, F.; Zhang, Q.; Zhou, Z.; Yi, T.; Huang, C. Versatile synthesis strategy for carboxylic acid-functionalized upconverting nanophosphors as biological labels. *J. Am. Chem. Soc.* **2008**, *130*, 3023–3029. [[CrossRef](#)] [[PubMed](#)]
11. Fujihara, S.; Kadota, Y.; Kimura, T. Role of organic additives in the sol-gel synthesis of porous CaF₂ anti-reflective coatings. *J. Sol-Gel Sci. Technol.* **2002**, *24*, 147–154. [[CrossRef](#)]
12. McKeever, S.W.S.; Brown, M.D.; Abbundi, R.J.; Chan, H.; Mathur, V.K. Characterization of optically active sites in CaF₂: Ce, Mn from optical spectra. *J. Appl. Phys.* **1986**, *60*, 2505–2510. [[CrossRef](#)]
13. Fukuda, Y. Thermoluminescence in sintered CaF₂:Tb. *J. Radiat. Res.* **2002**, *43*, S67–S69. [[CrossRef](#)] [[PubMed](#)]

14. Pote, S.S.; Joshi, C.P.; Moharil, S.V.; Muthal, P.L.; Dhopte, S.M. Luminescence of Ce³⁺ in Ca_{0.65}La_{0.35}F_{2.35} host. *J. Lumin.* **2010**, *130*, 666–668. [[CrossRef](#)]
15. Cazorla, C.; Errandonea, D. Superionicity and polymorphism in calcium fluoride at high pressure. *Phys. Rev. Lett.* **2014**, *113*, 235902. [[CrossRef](#)] [[PubMed](#)]
16. Sinclair, D.C.; West, A.R. Impedance and modulus spectroscopy of semiconducting BaTiO₃ showing positive temperature coefficient of resistance. *J. Appl. Phys.* **1989**, *66*, 3850–3856. [[CrossRef](#)]
17. Sinclair, D.C.; Adams, T.B.; Morrison, F.D.; West, A.R. CaCu₃Ti₄O₁₂: One-step internal barrier layer capacitor. *Appl. Phys. Lett.* **2002**, *80*, 2153–2155. [[CrossRef](#)]
18. Dutta, S.; Choudhary, R.N.P.; Sinha, P.K.; Thakur, A.K. Microstructural studies of (PbLa)(ZrTi)O₃ ceramics using complex impedance spectroscopy. *J. Appl. Phys.* **2004**, *96*, 1607–1613. [[CrossRef](#)]
19. Hsu, H.S.; Huang, J.C.A.; Chen, S.F.; Liu, C.P. Role of grain boundary and grain defects on ferromagnetism in Co: ZnO films. *Appl. Phys. Lett.* **2007**, *90*, 102506. [[CrossRef](#)]
20. Dualeh, A.; Moehl, T.; Tetreault, N.; Teuscher, J.; Gao, P.; Nazeeruddin, M.K.; Gratzel, M. Impedance spectroscopic analysis of lead iodide perovskite-sensitized solid-state solar cells. *ACS Nano* **2013**, *8*, 362–373. [[CrossRef](#)] [[PubMed](#)]
21. Huggins, R.A. Simple method to determine electronic and ionic components of the conductivity in mixed conductors: A review. *Ionics* **2002**, *8*, 300–313. [[CrossRef](#)]
22. Teraoka, Y.; Zhang, H.; Okamoto, K.; Yamazoe, N. Mixed ionic-electronic conductivity of La_{1-x}Sr_xCo_{1-y}Fe_yO_{3-δ} perovskite-type oxides. *Mater. Res. Bull.* **1988**, *23*, 51–58. [[CrossRef](#)]
23. Riess, I. Measurements of electronic and ionic partial conductivities in mixed conductors, without the use of blocking electrodes. *Solid State Ionics* **1991**, *44*, 207–214. [[CrossRef](#)]
24. Riess, I. Review of the limitation of the Hebb-Wagner polarization method for measuring partial conductivities in mixed ionic electronic conductors. *Solid State Ion.* **1996**, *91*, 221–232. [[CrossRef](#)]
25. Adler, S.B.; Lane, J.; Steele, B. Electrode kinetics of porous mixed-conducting oxygen electrodes. *J. Electrochem. Soc.* **1996**, *143*, 3554–3564. [[CrossRef](#)]
26. Riess, I. Mixed ionic–electronic conductors—Material properties and applications. *Solid State Ion.* **2003**, *157*, 1–17. [[CrossRef](#)]
27. Cui, X.Y.; Hu, T.J.; Wang, J.S.; Zhang, J.K.; Zhao, R.; Li, X.F.; Yang, J.H.; Gao, C.X. Mixed conduction in BaF₂ nanocrystals under high pressure. *RSC Adv.* **2017**, *7*, 12098–12102. [[CrossRef](#)]
28. Cui, X.Y.; Hu, T.J.; Wang, J.S.; Zhang, J.K.; Li, X.F.; Yang, J.H.; Gao, C.X. High pressure impedance spectroscopy of SrF₂ nanocrystals. *High Press. Res.* **2017**, *37*, 312–318. [[CrossRef](#)]
29. Hu, T.J.; Cui, X.Y.; Wang, J.S.; Zhang, J.K.; Li, X.F.; Yang, J.H.; Gao, C.X. Transport properties of mixing conduction in CaF₂ nanocrystals under high pressure. *Chin. Phys. B* **2018**, *27*, 016401. [[CrossRef](#)]
30. Mao, H.K.; Bell, P.M. High-pressure physics: The 1-megabar mark on the ruby R1 static pressure scale. *Science* **1976**, *191*, 851–852. [[CrossRef](#)] [[PubMed](#)]
31. Errandonea, D.; Muñoz, A.; Gonzalez-Platas, J. Comment on “High-pressure X-ray diffraction study of YBO₃/Eu³⁺, GdBO₃, and EuBO₃: Pressure-induced amorphization in GdBO₃” [J. Appl. Phys. 115, 043507 (2014)]. *J. Appl. Phys.* **2014**, *115*, 216101. [[CrossRef](#)]
32. Errandonea, D.; Segura, A.; Martínez-García, D.; Muñoz-San Jose, V. Hall-effect and resistivity measurements in CdTe and ZnTe at high pressure: Electronic structure of impurities in the zinc-blende phase and the semimetallic or metallic character of the high-pressure phases. *Phys. Rev. B* **2009**, *79*, 125203. [[CrossRef](#)]
33. Wang, J.S.; Hao, J.; Wang, Q.S.; Jin, Y.X.; Li, F.F.; Liu, B.; Li, Q.J.; Liu, B.B.; Cui, Q.L. Pressure-induced structural transition in CaF₂ nanocrystals. *Phys. Status Solidi B* **2011**, *248*, 1115–1118. [[CrossRef](#)]
34. Wang, Q.L.; Liu, C.L.; Gao, Y.; Ma, Y.Z.; Han, Y.H.; Gao, C.X. Mixed conduction and grain boundary effect in lithium niobate under high pressure. *Appl. Phys. Lett.* **2015**, *106*, 132902. [[CrossRef](#)]

